PAPER • OPEN ACCESS

Interface engineering of an electrospun nanofiber-based composite cathode for intermediate-temperature solid oxide fuel cells

To cite this article: Seo Ju Kim *et al* 2023 *Int. J. Extrem. Manuf.* **5** 015506

View the article online for updates and enhancements.

You may also like

- Material embrittlement in high strain-rate loading
  Xiuxuan Yang and Bi Zhang

- Surface modification and functionalization by electrical discharge coating: a comprehensive review
  Pay Jun Liew, Ching Yee Yap, Jingsi Wang et al.

- Advances in micro cutting tool design and fabrication
  John O'Hara and Fengzhou Fang

Interface engineering of an electrospun nanofiber-based composite cathode for intermediate-temperature solid oxide fuel cells

Seo Ju Kim[1,3]**, Deokyoon Woo**[1,3]**, Donguk Kim**[1]**, Tae Kyeong Lee**[1]**, Jaeyeob Lee**[1] **and Wonyoung Lee**[1,2,*] (ID)

[1] School of Mechanical Engineering, Sungkyunkwan University, Suwon, Kyunggi-do 16419, Republic of Korea
[2] SKKU Institute of Energy Science and Technology (SIEST), Sungkyunkwan University, Suwon 16419, Republic of Korea

E-mail: leewy@skku.edu

CrossMark

Abstract

Sluggish oxygen reduction reaction (ORR) kinetics are a major obstacle to developing intermediate-temperature solid-oxide fuel cells (IT-SOFCs). In particular, engineering the anion defect concentration at an interface between the cathode and electrolyte is important for facilitating ORR kinetics and hence improving the electrochemical performance. We developed the yttria-stabilized zirconia (YSZ) nanofiber (NF)-based composite cathode, where the oxygen vacancy concentration is controlled by varying the dopant cation (Y_2O_3) ratio in the YSZ NFs. The composite cathode with the optimized oxygen vacancy concentration exhibits maximum power densities of 2.66 and 1.51 W cm^{-2} at 700 and 600 °C, respectively, with excellent thermal stability at 700 °C over 500 h under 1.0 A cm^{-2}. Electrochemical impedance spectroscopy and distribution of relaxation time analysis revealed that the high oxygen vacancy concentration in the NF-based scaffold facilitates the charge transfer and incorporation reaction occurred at the interfaces between the cathode and electrolyte. Our results demonstrate the high feasibility and potential of interface engineering for achieving IT-SOFCs with higher performance and stability.

Supplementary material for this article is available online

Keywords: solid oxide fuel cells, nanofiber, infiltration, oxygen reduction reactions, oxygen vacancy

---

[3] These authors are contributed equally to this work.
[*] Author to whom any correspondence should be addressed.

1. Introduction

A solid oxide fuel cell (SOFC) attracts much attention as a promising green-energy system because of its high efficiency and fuel flexibility with no harmful by-products. SOFCs usually operate at high temperatures (800 °C–1000 °C), where the ionic conductivity of the ceramic electrolyte meets the required level and the oxygen reduction reaction (ORR) in the cathode is facilitated [1, 2]. However, such high operation temperatures are costly and cause considerable thermal degradation, limiting their wider commercialization [3–5]. Lowering the operation temperature, however, decreases the performance exponentially, mainly because the polarization resistances associated with the ORR at the cathode significantly increase due to their high activation energy [6–10]. Therefore, extensive and intensive investigations over the last decades have sought to lower the operating temperature to an intermediate temperature range (IT, 600 °C–800 °C), without significant performance loss, by developing highly reactive cathodes [11, 12].

Composite cathodes improve the ORR kinetics in IT operations effectively because the ORR mostly occurs at interfaces between the cathode and electrolyte [6]. In most composite cathodes, the structural and chemical properties were engineered to increase the number of reaction sites or the triple phase boundaries (TPBs) where oxygen ions, electrons, and gas meet by controlling the particle-size distribution from a few tens of nanometers to the single-atom level [13–15]; the strain state of the cathode materials (tensile or compressive) [16]; and the anion defect concentration at the electrolyte surface or interface between the cathode and electrolyte [17, 18]. In particular, oxygen-related defect chemistry at the interface between the cathode and electrolyte plays an important role in the overall ORR kinetics (e.g. charge transfer, ion incorporation, ion transport, and gas adsorption) because it affects the reaction barrier significantly [19–21]. Moreover, desired oxygen vacancy concentrations could differ for the ORR at the interface and the ion conduction in the bulk electrolyte [22, 23]. Therefore, composite cathodes with different oxygen vacancy concentrations at the interface and in the bulk have been developed by controlling the thermal treatment temperature [24–27] and the cation dopant ratio [28, 29], demonstrating improved polarization resistances and cell performance. However, these approaches have been demonstrated using a flat electrolyte surface prepared by vacuum deposition [24–27] and a conventional powder scaffold by infiltration [28–30], resulting in limited improvement in the electrochemical performance, especially in IT operations.

Another approach involves employing low-dimensional nanostructures for the cathode scaffold for the increasing the number of reaction sites. Recently, electrospun nanofibers (NFs) have been demonstrated as cathode structures because of their high specific surface area, which provides enlarged reaction sites, and their porous but connected network, which provides fast ionic and electronic pathways along the axial direction [31, 32]. In addition, the electrospinning process allows the precise control of a wide variety of NF structures, e.g. with diameters ranging from 200 to 800 nm [33], shapes ranging from solid to hollow [34, 35], and including single and core–shell NFs [36–39]. In particular, composite NFs can be fabricated relatively simply by using a mixed suspension [36, 40], a co-axial nozzle [37], and by subsequent infiltration [41] for enlarging the reaction area. However, these approaches require a relatively high sintering temperature (>1000 °C) to achieve sufficient bonding with flat substrates, owing to the high aspect ratio of NFs. This results in the loss of their structural advantages [34, 37, 42] and a lower improvement in polarization resistance and cell performance than expectations. Therefore, this motivates developing a NF-based electrode fabrication process to fully utilize the advantages of NFs and achieve high performance IT-SOFCs.

This study demonstrates the use of composite cathode structure with an NF-based scaffold and infiltrated electrode nanoparticles to effectively extend the reaction area. In addition, the oxygen vacancy concentration of the NF-based scaffold was controlled by varying the Y_2O_3 doping ratio in the electrolyte material, $(Y_2O_3)_x(ZrO_2)_{1-x}$ (yttria-stabilized zirconia (YSZ)). While structural properties remained unaffected, the oxygen vacancy concentration in the NF-based scaffold increased monotonically as the controlled dopant cation ratio varied from 0 to 16 mol%. A composite cathode with 12 mol% of Y_2O_3 in YSZ NFs exhibits a remarkable performance of 2.66 W cm^{-2} and 1.51 W cm^{-2} at 700 and 600 °C, respectively, with outstanding thermal stability i.e. almost no degradation at 700 °C over 500 h under 1.0 A cm^{-2}. Electrochemical impedance spectroscopy (EIS) and distribution of relaxation time (DRT) analysis confirmed that the high oxygen vacancy concentration in the NF-based scaffold substantially facilitates the charge transfer and ion incorporation reactions at TPBs. Our results demonstrate how a precisely designed interface between the cathode and electrolyte significantly improves the electrochemical performance, thereby raising the possibility of operating SOFCs in the IT regime with high performance and stability.

2. Experimental methods

2.1. YSZ NF synthesis

A polymer solution must be prepared before synthesizing the YSZ NFs. Polyacrylonitrile (PAN, $MW = 150\,000$, Sigma Aldrich) was dissolved in N,N-dimethylformamide (DMF, Alfa Aesar) to 10 wt% and stirred with a magnetic bar continuously on a hot plate at 70 °C for 24 h to ensure complete dissolution. Then, yttrium nitrate hexahydrate $Y(NO_3)_2 \cdot 6H_2O$ (Sigma Aldrich) and zirconium acetate hydroxide $(CH_3CO_2)_X Zr(OH)_Y$ (Sigma Aldrich) were added into the polymer solution to a total cation concentration of 0.1 M and stirred at 80 °C overnight to fully dissolve the precursor. The Y_2O_3 doping ratio in the YSZ NFs was varied by controlling the ratio of yttrium nitrate hexahydrate and zirconium acetate hydroxide for the chemical composition of $(Y_2O_3)_x(ZrO_2)_{1-x}$ ($x = 0$, 0.04, 0.08, 0.12, and 0.16). For the

electrospinning process, the obtained solution was loaded into a 10 ml plastic syringe and injected into a 27-gauge nozzle with a 4 ml h^{-1} flow rate. An electric field of 1.2 kV cm^{-1} was applied to the metal nozzle, and the Al-foil collector was grounded. The distance between the Al foil collector and the metal nozzle tip was fixed at 10 cm. The as-spun YSZ NF mat was heated to 280 °C (ramping rate of 5 °C min^{-1}), maintained for 1 h, and sintered at 1000 °C (ramping rate of 1 °C min^{-1}) for 3 h after 280 °C in air.

2.2. Single-cell fabrication

To measure the electrochemical performance depending on the Y_2O_3 doping ratio in YSZ NF, Ni-YSZ based anode supported cells were prepared. NiO (Fuel Cell Materials), YSZ (Tosoh), and poly(methyl methacrylate) (PMMA, Alfa Aesar) powders were mixed into 20 ml of ethanol with a weight ratio of 6:4:1.25. Then, 0.3 ml of the powder dispersant KD-6 (Croda) and the binder polyvinyl butyral (Sigma Aldrich) were added to the dispersion solution. The subsequent ball-milling process was conducted for 24 h. After the drying process of the NiO-YSZ anode powder was completed, dense anode disks were prepared under 20 MPa pressure to produce 700 μm-thick circular pellets, followed by the sintering at 1000 °C (ramping rate of 3 °C min^{-1}) for 3 h. The anode functional layer (AFL) and electrolyte layer were formed by spin-coating. The AFL solution was prepared using an 8 g mixture of NiO and YSZ powders (6:4 weight ratio) dispersed into 20 ml of ethanol, adding 0.2 g of ethyl cellulose (50 cps, Sam Chun) as a binder and 0.12 g of KD-6 as a dispersant. The YSZ electrolyte solution was prepared identically with the AFL solution using YSZ powder only. The AFL (25 μm) and electrolyte (4 μm) were deposited onto the anode pellet. The AFL and YSZ electrolyte layers were synthesized with a spin-coating process and these were co-sintered at 1400 °C for 3 h for sufficient densification of the YSZ electrolyte. The composite cathode was fabricated as follows. A 5 μm-thick adhesion layer was screen-printed onto the electrolyte using a mixture of sintered YSZ powder and ink vehicle (Fuel cell Materials) (1:1 weight ratio), and sintered at 1200 °C for 3 h. A mixture of YSZ NFs and ink vehicle having a weight ratio of 1:10 was screen-printed onto the YSZ powder to obtain a ~25 μm-thick scaffold, and sintered at 800 °C for 3 h. To form the LSM nanoparticles onto the YSZ NFs, 0.8 M of LSM precursor solution was prepared. Each cation precursor (La(NO$_3$)$_3$ · 6H$_2$O (Sigma Aldrich), Sr(NO$_3$)$_2$ (Sigma Aldrich), Mn(NO$_3$)$_2$ · 6H$_2$O (Alfa Aesar)) was dissolved in N,N-dimethylformamide (DMF, Alfa Aesar) with a molar ratio of 0.8:0.2:1.0 and Triton X-100 (Sigma Aldrich) was used as surfactant to achieve the desired stoichiometry of La$_{0.8}$Sr$_{0.2}$MnO$_3$. After injecting 21 ml of LSM solution into the cathode scaffold, the infiltration solution was dried at 150 °C in the air for 1 h and the single cell was sintered at 800 °C for 3 h to form the LSM particles. For current collecting the cathode side, platinum paste (5542, ESL) was screen-printed and the sintering process was conducted at 800 °C for 1 h.

2.3. Characterization

Scanning electron microscopy (SEM, JEOL, JSM700F) was used to analyze the morphological properties of the NFs and electrodes. To investigate the crystalline phase and phase formation, x-ray diffraction (XRD, Bruker Corporation, D8 Advance), with Cu Kα radiation ($\lambda = 1.5406$ Å) at room temperature, was employed. To determine the chemical composition and oxygen defect structures of YSZ NFs, x-ray photoelectron spectroscopy (XPS, ESCA Lab 250 XPS spectrometer, VG Scientific Instruments) with a monochromatic Al K$_\alpha$ source was employed. The specific surface area of the YSZ NF was obtained through the Brunauer Emmett Teller (BET) isothermal technique with nitrogen adsorption using a surface-area analyzer (BELSORP mini-II, Microtrac BEL Japan, Inc.). To evaluate the electrochemical characteristics including the EIS and current–voltage curves (I–V curves) of a single cell, a potentiostat (Interface 1010E, Gamry Instruments) was used. The single-cell test was conducted with a bias of 50 mV in a temperature range of 600 °C–750 °C and a frequency range of 10^5–10^6 Hz. To identify the ORR steps in detail, the DRT and EIS fitting was conducted.

3. Results & discussion

Figures 1(a) and (b) show a schematic and a cross-sectional SEM image of the overall single-cell configuration used for electrochemical testing. The structure is Ni-YSZ anode/Ni-YSZ anode functional layer/YSZ electrolyte/LSM-infiltrated YSZ NF-based composite cathode. The porous YSZ powder layer (of thickness ~5 μm) serves as a bonding layer between the YSZ electrolyte and the YSZ NF scaffold as it provides sufficient adhesion between the smooth electrolyte and YSZ NF scaffold with the high aspect ratio [34, 40]. To exclusively investigate the effects of the oxygen vacancy concentration of YSZ NFs on the electrochemical performance, all cell components were identically fabricated, except for a varying cation doping ratio in the YSZ NFs. To maximize the interfaces between the cathode and electrolyte, the wet-chemical based infiltration process with LSM precursors was conducted onto the YSZ NF scaffold and YSZ bonding layer. Figure 1(c) shows the uniformly coated LSM nanoparticles (size 30–40 nm) from the YSZ NF scaffold to the YSZ bonding layer, without a noticeable difference in the particle size and coverage. The cation doping ratio in the YSZ NFs was controlled by varying the precursor amount of Y_2O_3 and ZrO_2 in the electrospinning solution as 0:100, 4:96, 8:92, 12:88, and 16:84, denoted as 0 YSZ, 4 YSZ, 8 YSZ, 12 YSZ, and 16 YSZ, respectively, according to the Y_2O_3 mol% in the YSZ. All YSZ NFs, after thermal treatment at 1000 °C, showed similar structural properties regardless of the cation doping ratio: the solid-type NFs with a diameter of 162.0 $\pm$ 6.8 nm and specific surface area of 10.4 $\pm$ 0.4 m^2 g^{-1}, as confirmed by SEM images and BET measurements, respectively (figure S1). Insignificant differences in the structural properties of YSZ
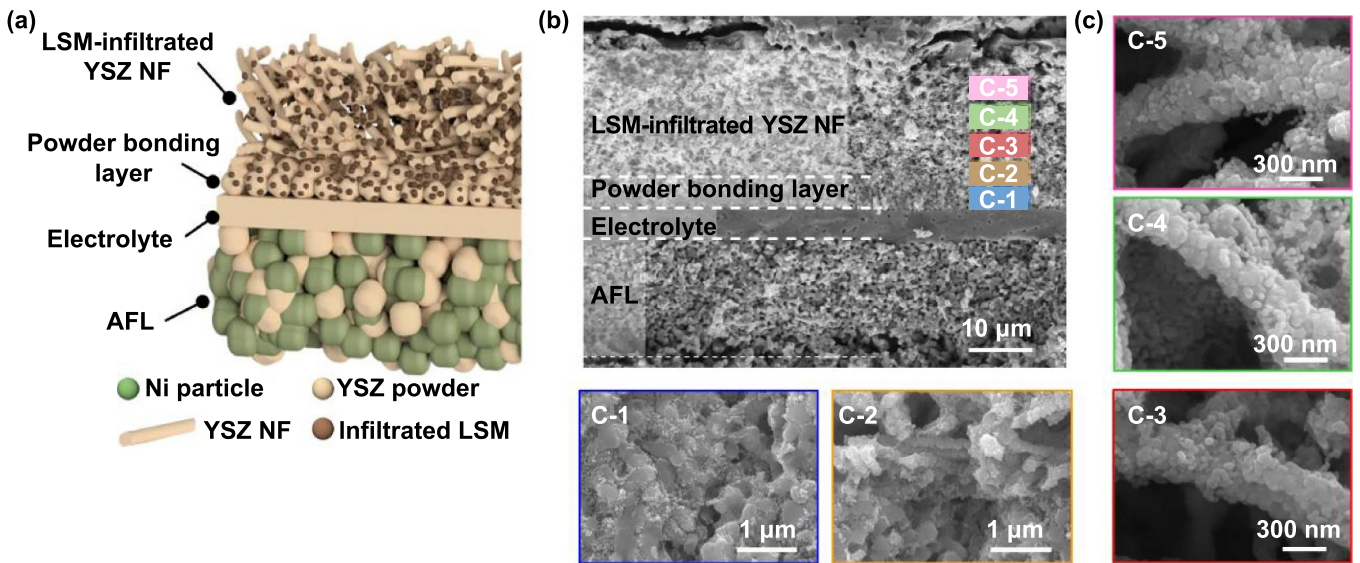
Figure 1. (a) Schematic and (b) SEM image of an Ni-YSZ anode supported single cell with a YSZ NF-based composite cathode, and (c) SEM images of the (c-1) YSZ bonding layer, (c-2) the interface between the YSZ bonding layer and YSZ NF scaffold, and the (c-3) bottom (c-4) middle, and (c-5) top of YSZ NF scaffold.
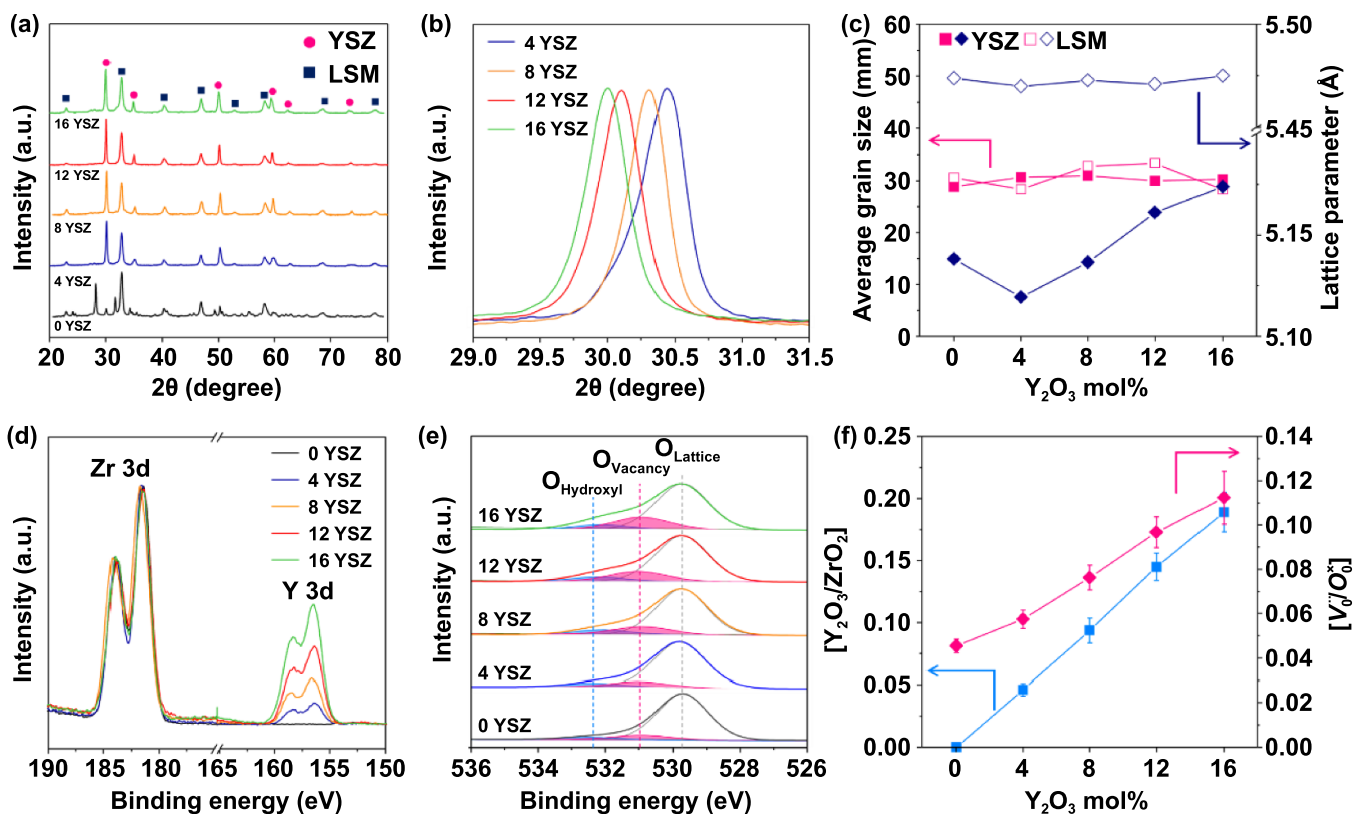

Figure 2. XRD patterns of the LSM-infiltrated YSZ NFs with Y2O3 mol% varying from 0 to 16 mol% (a) in the 2θ range of $20°$–$80°$ and (b) in the (111) direction of YSZ. (c) Average grain size and lattice parameter of the YSZ NFs and infiltrated LSM. XPS spectra of the YSZ NF scaffolds of (d) normalized Y 3d peaks by Zr 3d peaks and (e) O 1 s spectra. (e) Cation ratio ($[Y_2O_3/ZrO_2]$) and oxygen vacancy concentration ($\left[V_O^{\cdot\cdot}/O_O^{\times}\right]$) as functions of Y2O3 mol%.

NFs indicate negligible effects of the cation doping ratio on the reaction sites in the scaffold.

The structural and chemical characteristics of YSZ NFs that can determine the overall electrochemical performance were analyzed as functions of the Y_2O_3 mol% in the YSZ NF scaffolds. Figure 2(a) shows the XRD patterns of all LSM-infiltrated YSZ NFs with different Y_2O_3 mol% values, over the 2θ range of $20°$–$80°$, verifying the fluorite phase
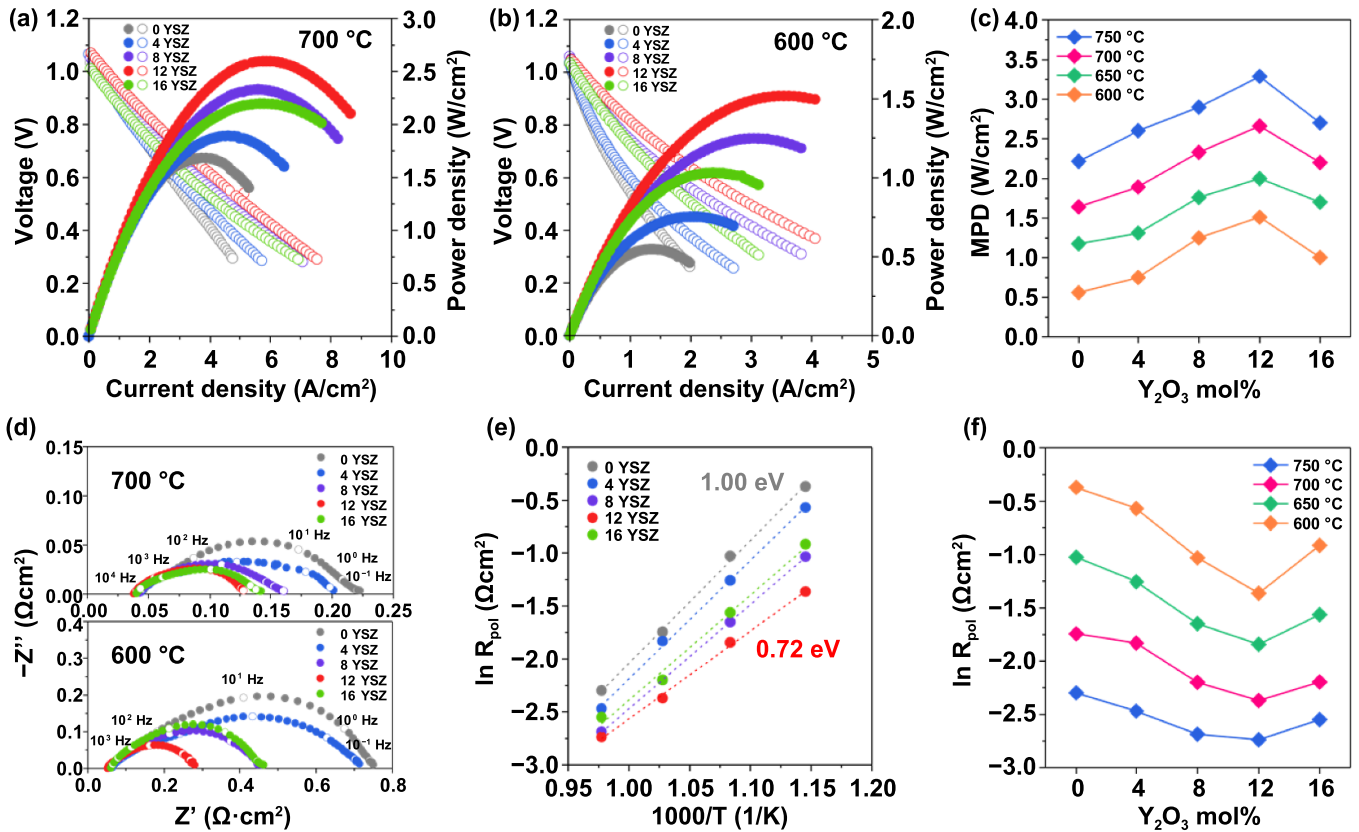
Figure 3. IVP curves of the LSM-infiltrated YSZ NFs cells with controlled Y_2O_3 mol% in the range 0 –16 mol% at (a) 700 °C and (b) 600 °C. (c) MPDs for all the cells, in the temperature range 600 °C–750 °C. (d) Nyquist curves measured at 700 and 600 °C under OCV condition. (e) Arrhenius plots and (f) R_{pol} for all the cells, at a temperature range of 600 °C–750 °C.

of YSZ NF scaffolds and the perovskite phase of the infiltrated LSM nanoparticles without their unnecessary reactions. 0 YSZ (ZrO_2) displayed the monoclinic phase after thermal treatment at 1000 °C, instead of the cubic phase in other YSZ NFs [43]. Figure 2(b) shows the representative YSZ peaks for 2θ between 29.5° and 31.0° in the (111) direction, exhibiting a noticeable shift toward smaller angles with increasing Y_2O_3 mol%. This monotonic peak shift indicates that the lattice parameters increased with the Y_2O_3 mol% because of greater ionic radius of Y^{3+} (93 pm) than that of Zr^{4+} (80 pm). This confirms the desired control of the cation doping ratio in YSZ NFs [44]. Figure 2(c) shows the lattice parameters and the average grain sizes of the YSZ NFs and infiltrated LSM nanoparticles, determined according to Y_2O_3 mol%. The average grain sizes of the YSZ NFs (30.2 ± 0.8 nm) and infiltrated LSM nanoparticles (30.7 ± 2.1 nm) were independent of Y_2O_3 mol% in the YSZ NFs.

The chemical characteristics of YSZ NFs were investigated through XPS analysis as functions of Y_2O_3 mol% in the YSZ NF scaffolds. Figure 2(d) shows the increase in the relative intensity of the Y 3d peak to that of the Zr 3d peak with the higher Y_2O_3 mol% in YSZ NF scaffolds. The cation ratio calculated from the XPS result confirmed that the chemical composition of $[Y_2O_3/ZrO_2]$ was precisely controlled as shown in figure 2(f). Since the oxygen vacancy is formed from the charge imbalance caused by the substituted trivalent dopant

cation with tetravalent host cation in the fluorite-structured oxide according to equation (1), the higher Y_2O_3 mol% in the YSZ NFs should accompany the further formation of oxygen vacancies.

$$Y_2O_3 \underset{Zr}{\rightarrow} 2Y_{Zr}^{'} + V_O^{\bullet\bullet} + 3O_O^{\times}. \tag{1}$$
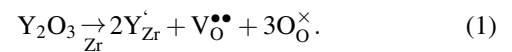
Figure 2(e) shows the O 1 s spectra composed of three different binding states: $O_{lattice}$ (529.32 eV), $O_{vacancy}$ (530.95 eV), and $O_{hydroxyl}$ (532.11 eV). The detailed fit results are listed in table S1. The intensity ratio $\left[V_O^{\bullet\bullet}/O_O^{\times}\right]$ of $O_{vacancy}$ to $O_{lattice}$ (which corresponds to the oxygen vacancy concentration) increases monotonically as Y_2O_3 mol% in the YSZ NFs increases from 0 to 16 mol%, as shown in figure 2(f). The contribution of $O_{hydroxyl}$ on the YSZ surface, indicating OH^- adsorption due to atmospheric exposure, is similar in all YSZ NFs with the intensity ratio of $O_{hydroxyl}$ to $O_{lattice}$ of 0.082 ± 0.011. Therefore, we conclude that varying Y_2O_3 mol% in YSZ NFs controls the oxygen vacancy concentration precisely, while maintaining the similar structural characteristics of the YSZ NFs and infiltrated LSM nanoparticles.

To examine the effects of Y_2O_3 mol% in YSZ NF scaffolds on fuel cell performance, *I–V–P* and EIS analyses were conducted in a Ni-YSZ-based anode-supported single cell configuration. Figures 3(a)–(c) show that the electrochemical
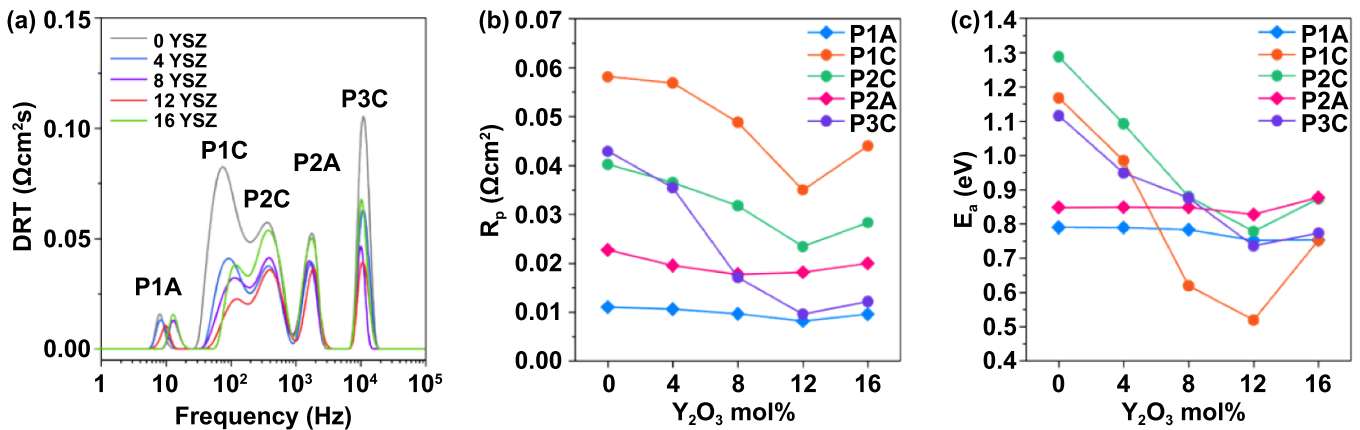
Figure 4. Electrochemical analyses of the LSM-infiltrated YSZ NFs cells with controlled Y_2O_3 mol%. Measurements were conducted at 700 °C: (a) DRT analysis; (b) EIS fitting results for P1A, P1C, P2C, P2A, and P3C as functions of Y_2O_3 mol%; and (c) correlation of activation energy and Y_2O_3 mol%.

performance increases with the oxygen vacancy concentration in the YSZ NF scaffolds in the temperature range of 600 °C–750 °C. The highest maximum power density (MPD) was obtained in cell 12 YSZ: 2.66 W cm^{-2} at 700 °C and 1.55 W cm^{-2} at 600 °C. Figure 3(d) shows the Nyquist plots measured at 700 and 600 °C, attributing the improved performance to the substantial reduction of polarization resistance (R_{pol}) with increasing Y_2O_3 mol%, while ohmic resistance (R_{ohm}) remains almost identical, for example, 0.039 ± 0.003 Ωcm^2 at 700 °C and 0.058 ± 0.003 Ωcm^2 at 600 °C. Representatively, cell 12 YSZ has a R_{pol} of 0.094 Ωcm^2 at 700 °C and 0.25 Ωcm^2 at 600 °C. Figure 3(e) shows Arrhenius plots of R_{pol} in the temperature range 600 °C–750 °C, showing a decrease in activation energy (E_a) with increasing Y_2O_3 mol% from 1.00 eV in cell 0 YSZ to 0.72 eV in cell 12 YSZ. E_a values for R_{ohm} are almost identical at 0.25 ± 0.03 eV in all cells, as shown in figure S2. Figure 3(f) plots R_{pol} as a function of Y_2O_3 mol%, confirming the decrease in R_{pol} with increasing Y_2O_3 mol% over the temperature range 600 °C–750 °C. Notably, the smallest R_{pol} and the highest MPD were obtained in cell 12 YSZ, although YSZ with 8 Y_2O_3 mol% has been widely used because of its highest ionic conductivity [23]. In addition, cell 16 YSZ shows a greater R_{pol} and a lower MPD than cell 12 YSZ, despite the higher Y_2O_3 mol%. These results signify the importance of precise defect engineering at the interface for promoting ORR kinetics and maximizing electrochemical performance without deteriorating ion conduction.

The effects of Y_2O_3 mol% in the YSZ NF scaffolds on R_{pol} were further investigated with a DRT analysis and by EIS fitting using equivalent circuit models. DRT analysis quantitatively assesses elementary reactions and the contribution of associated reaction resistance [45]. Figure 4(a) shows the DRT analysis result for LSM-infiltrated YSZ NFs cells with varying Y_2O_3 mol% at 700 °C. Five distinct peaks were identified in the DRT spectra, corresponding to two anode reactions (P1A in 5×10^0–2×10^1 Hz and P2A in 10^3–3×10^3 Hz), which are assigned to hydrogen gas diffusion in the anode

and charge transfer in the anode functional layer; and three cathode reactions (P1C in 3×10^1–2×10^2 Hz, P2C in 3×10^2–10^3 Hz, and P3C in 6×10^3–2×10^4 Hz), which are assigned to charge transfer at TPBs, oxygen species diffusion, and oxygen ion incorporation in the interface between the cathode and electrolyte, respectively [46]. Figure 4(b) shows the R_{pol} values that were fitted based on DRT analysis as a function of Y_2O_3 mol%. Both analyses reveal the substantial reduction in R_{pol} associated with cathode reactions (P1C, P2C, and P3C) as Y_2O_3 mol% increases, compared with the insignificant change in those associated with anode reactions (P1A and P2A). Moreover, E_a for each reaction (calculated from the Arrhenius plots in figure S2) shows a tendency similar to that of R_{pol}. Figure 4(c) plots the E_a derived from the R_{pol} values fitted based on DRT analysis, as a function of Y_2O_3 mol%. This reveals that E_a for the cathode reactions (P1C, P2C, and P3C) substantially decreases with Y_2O_3 mol%, while E_a for anode reactions (P1A and P2A) remains unchanged. In particular, cell 12 YSZ shows the most pronounced reduction in R_{pol} and E_a associated with cathode reactions, consistent with the total R_{pol} and E_a in figures 3(e) and (f). The facilitation of ORR kinetics by the higher Y_2O_3 mol% can be attributed to the higher oxygen vacancy concentration at the interfaces between the cathode and electrolyte because of the lower activation energy for oxygen charge transfer and ion incorporation reaction at and near the oxygen vacancy [26]. However, an oxygen vacancy concentration in excess of the optimum value can deteriorate the ORR kinetics. This is shown with cell 16 YSZ, which has a higher Y_2O_3 mol% but lower R_{pol} and E_a associated with cathode reactions, compared with those of cell 12 YSZ. This is because not only the concentration but also the location of oxygen vacancies is important in ORR kinetics. Reportedly, an oxygen vacancy located between dopant cations has a low activity for oxygen adsorption and diffusion [47, 48]. Therefore, these results confirm the need to precisely control the defect concentration at the interface and its specific impact on ORR kinetics.
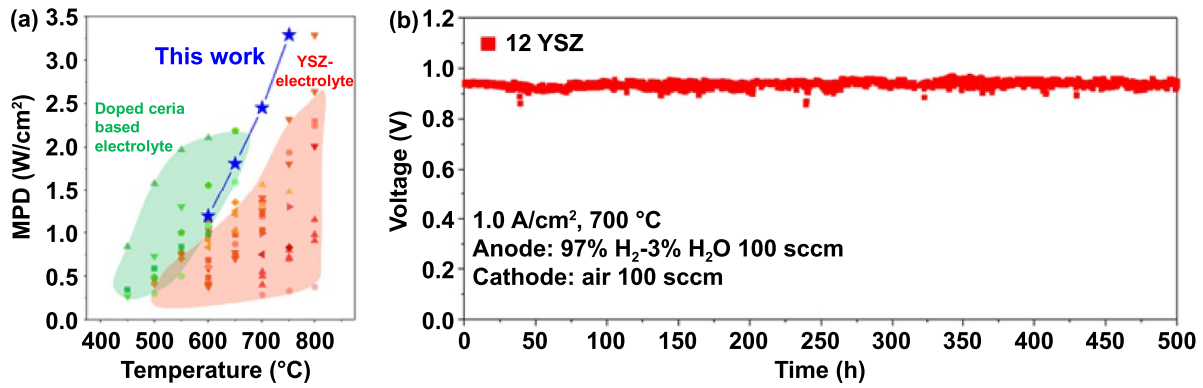
Figure 5. (a) MPD comparison with previous reports. (b) Stability test at 700 °C for 500 h under 1.0 A cm^{-2}.

Table 1. Comparing the stability of LSM-infiltrated YSZ NFs cell and literature results.

Cell configuration	Operation temperature (°C)	Current density (A cm^{-2})	Degradation rate	References
Ni-YSZ|YSZ| LSM-infiltrated YSZ NF	700	1.0	0.2%/500 h	This study
NiO−YSZ|YSZ|YSZ-LSM powder	600	0.4	50%/500 h	[46]
NiO−YSZ|YSZ|YSZ-LSM infiltrated YSZ			1%/500 h	
NiO−YSZ|YSZ|GDC|LSCF powder	600	0.6	6.3%/200 h	[50]
NiO−YSZ|YSZ|GDC|LSCF NF		0.65	∼0%/200 h	
NiO−YSZ|YSZ|GDC|LSCF/CeO2 NF		0.9	∼0%/200 h	
NiO−YSZ|YSZ|GDC|SSC infiltrated (LSCF-GDC)	750	0.5	∼0%/200 h	[51]
NiO−YSZ|YSZ|GDC|GDC-PBSCF|PBSCF	700	0.3	1.98%/310 h	[52]
NiO−YSZ|YSZ|GDC|LSCF powder	650	0.4	∼0%/100 h	[53]
Ni-GDC/GDC/BSCF-GDC	550	1.0	5.6%/250 h	[39]
		0.5	0.6%/50 h	
Ni-GDC/GDC/PBSC	550	1.5	11.54%/225 h	[32]
Ni-SDC/SDC/SCFN-GDC	700	0.6	8.83%/20 h	[54]
Ni-GDC/GDC/NBCaCO	550	0.6	47.9%/150 h	[55]
Ni-GDC/GDC/PBCCF05-GDC	550	0.07	5.47%/30 h	[56]
Ni-GDC/GDC/PBCCO-GDC	550	0.6	28.2%/30 h	

Lastly, to evaluate the performance and stability of LSM-infiltrated YSZ NFs cells, we compared the MPD values and degradation rate obtained in this study with published values, as shown in figure 5 and table 1. MPD values for cell 12 YSZ are significantly higher than those of YSZ electrolyte-based cells. They are even comparable to those of doped ceria electrolyte-based cells. Doped ceria materials such as gadolinia-doped ceria (GDC) and samaria-doped ceria (SDC) were developed as electrolytes of IT-SOFCs because of their high ionic conductivity (GDC: 0.0182 S cm^{-1} at 600 °C; YSZ: 0.0034 S cm^{-1} at 600 °C) and low activation energy (GDC: 0.64 eV; YSZ: 0.91 eV) [49]. However, unlike YSZ electrolyte, a doped ceria electrolyte typically displays practical drawbacks in terms of electrical leakage and thermal degradation, which deteriorate electrochemical performance and stability, as summarized in table 1. Figure 5(b) confirms the excellent thermal stability of cell 12 YSZ at 700 °C over 500 h under a current density of 1.0 A cm^{-2}, with a degradation rate of 0.2%/500 h. Therefore, our results demonstrate that the design principle of the LSM-infiltrated YSZ NF-based cells may overcome the low performance of YSZ electrolyte-based cells and the low stability of doped ceria electrolyte-based cells, enabling the operation of YSZ electrolyte-based cells at intermediate temperatures with high performance and stability.

4. Conclusion

We reported the YSZ NF-based composite cathodes with an optimized oxygen vacancy concentration to achieve the high performance and stability of IT-SOFCs. The oxygen vacancy concentration was elaborately controlled through the cation doping ratio in YSZ NFs. The strong correlation between the oxygen vacancy concentration and the polarization resistance associated with oxygen charge transfer and ion incorporation reactions at the cathode confirms the facilitation of ORR kinetics with enriched oxygen vacancies at the interfaces between the cathode and electrolyte. The YSZ NF-based composite cathode with the optimized oxygen vacancy concentration exhibits maximum power densities of 2.66 and 1.51 W cm^{-2} at 700 and 600 °C, respectively, with excellent thermal stability at 700 °C over 500 h under 1.0 A cm^{-2}. Our results provide important insight for developing IT-SOFCs with high performance and stability by defect engineering at the interfaces.

Acknowledgments

ORCID iD

Wonyoung Lee 🄳 https://orcid.org/0000-0002-1349-4017

References

[1] Brett D J L, Atkinson A, Brandon N P and Skinner S J 2008 Intermediate temperature solid oxide fuel cells *Chem. Soc. Rev.* **37** 1568–78

[2] Wachsman E D and Lee K T 2011 Lowering the temperature of solid oxide fuel cells *Science* **334** 935–9

[3] Connor P A *et al* 2018 Tailoring SOFC electrode microstructures for improved performance *Adv. Energy Mater.* **8** 1800120

[4] Ding D, Li X X, Lai S Y, Gerdes K and Liu M L 2014 Enhancing SOFC cathode performance by surface modification through infiltration *Energy Environ. Sci.* **7** 552–75

[5] Irvine J T S, Neagu D, Verbraeken M C, Chatzichristodoulou C, Graves C and Mogensen M B 2016 Evolution of the electrochemical interface in high-temperature fuel cells and electrolysers *Nat. Energy* **1** 15014

[6] Adler S B 2004 Factors governing oxygen reduction in solid oxide fuel cell cathodes *Chem. Rev.* **104** 4791–843

[7] Choi M, Lee J and Lee W 2018 Nano-film coated cathode functional layers towards high performance solid oxide fuel cells *J. Mater. Chem.* A **6** 11811–8

[8] Kim S J, Choi M, Lee J and Lee W 2020 Modifying defect structures at interfaces for high-performance solid oxide fuel cells *J. Eur. Ceram. Soc.* **40** 3089–97

[9] Choi M, Hwang S, Kim S J, Lee J, Byun D and Lee W 2019 Rational design of a metallic functional layer for high-performance solid oxide fuel cells *ACS Appl. Energy Mater.* **2** 4059–68

[10] Lee J, Hwang S, Ahn M, Choi M, Han S, Byun D and Lee J 2019 Enhanced interface reactivity by a nanowrinkled functional layer for intermediate-temperature solid oxide fuel cells *J. Mater. Chem.* A **7** 21120–7

[11] Kan W H, Samson A J and Thangadurai V 2016 Trends in electrode development for next generation solid oxide fuel cells *J. Mater. Chem.* A **4** 17913–32

[12] Gao Z, Mogni L V, Miller E C, Railsback J G and Barnett S A 2016 A perspective on low-temperature solid oxide fuel cells *Energy Environ. Sci.* **9** 1602–44

[13] Sato K, Iwata C, Kannari N and Abe H 2019 Highly accelerated oxygen reduction reaction kinetics in colloidal-processing-derived nanostructured lanthanum strontium cobalt ferrite/gadolinium-doped ceria composite cathode for intermediate-temperature solid oxide fuel cells *J. Power Sources* **414** 502–8

[14] Burye T E and Nicholas J D 2015 Nano-ceria pre-infiltration improves $La_{0.6}Sr_{0.4}Co_{0.8}Fe_{0.2}O_{3-x}$ infiltrated solid oxide fuel cell cathode performance *J. Power Sources* **300** 402–12

[15] Shin J *et al* 2020 Highly active and thermally stable single-atom catalysts for high-temperature electrochemical devices *Energy Environ. Sci.* **13** 4903–20

[16] Kim K, Koo B, Jo Y R, Lee S, Kim J K, Kim B J, Jung W C and Han J W 2020 Control of transition metal–oxygen bond strength boosts the redox ex-solution in a perovskite oxide surface *Energy Environ. Sci.* **13** 3404–11

[17] Zhu Y M, Liu X, Jin S G, Chen H J, Lee W, Liu M L and Chen Y 2019 Anionic defect engineering of transition metal oxides for oxygen reduction and evolution reactions *J. Mater. Chem.* A **7** 5875–97

[18] Develos-Bagarinao K, De Vero J, Kishimoto H, Ishiyama T, Yamaji K, Horita T and Yokokawa H 2018 Multilayered LSC and GDC: an approach for designing cathode materials with superior oxygen exchange properties for solid oxide fuel cells *Nano Energy* **52** 369–80

[19] Choi M, Koo J Y, Ahn M and Lee W 2017 Effects of grain boundaries at the electrolyte/cathode interfaces on oxygen reduction reaction kinetics of solid oxide fuel cells *Bull. Korean Chem. Soc.* **38** 423–8

[20] Cho G Y, Lee Y H, Yu W, An J and Cha S W 2019 Optimization of Y_2O_3 dopant concentration of yttria stabilized zirconia thin film electrolyte prepared by plasma enhanced atomic layer deposition for high performance thin film solid oxide fuel cells *Energy* **173** 436–42

[21] Lee H, Gwon O, Choi K, Zhang L J, Zhou J, Park J, Yoo J W, Wang J Q, Lee J H and Kim G 2020 Enhancing bifunctional electrocatalytic activities via metal d-band center lift induced by oxygen vacancy on the subsurface of perovskites *ACS Catal.* **10** 4664–70

[22] Kim J W, Jang D Y, Kim M, Jeong H, Kim N and Shim J H 2017 Compositional optimization of gadolinia-doped ceria treatment for enhanced oxygen reduction kinetics in low-temperature solid oxide fuel cells *Thin Solid Films* **624** 95–100

[23] Fergus J W 2006 Electrolytes for solid oxide fuel cells *J. Power Sources* **162** 30–40

[24] Lee W, Jung H J, Lee M H, Kim Y B, Park J S, Sinclair R and Prinz F B 2012 Oxygen surface exchange at grain boundaries of oxide ion conductors *Adv. Funct. Mater.* **22** 965–71

[25] Kim Y B, Park J S, Gür T M and Prinz F B 2011 Oxygen activation over engineered surface grains on YDC/YSZ interlayered composite electrolyte for LT-SOFC *J. Power Sources* **196** 10550–5

[26] Park J S, An J, Lee M H, Prinz F B and Lee W 2015 Effects of surface chemistry and microstructure of electrolyte on oxygen reduction kinetics of solid oxide fuel cells *J. Power Sources* **295** 74–78

[27] Bae J, Lim Y, Park J S, Lee D, Hong S, An J and Kim Y B 2016 Thermally-induced dopant segregation effects on the space charge layer and ionic conductivity of nanocrystalline gadolinia-doped ceria *J. Electrochem. Soc.* **163** F919–26

[28] Kim S J, Baek J, Choi M, Lee J and Lee W 2021 Controlling oxygen defect chemistry at electrolyte surface of intermediate temperature solid oxide fuel cells *J. Power Sources* **509** 230351

[29] Kim S J, Koo J Y, Mun T, Choi M and Lee W 2020 Tailoring defect chemistry at interfaces for promoted oxygen reduction reaction kinetics *J. Mater. Chem.* A **8** 23313–22

[30] Koo J Y, Mun T, Lee J, Choi M, Kim S J and Lee W 2020 Enhancement of oxygen reduction reaction kinetics using infiltrated yttria-stabilized zirconia interlayers at the electrolyte/electrode interfaces of solid oxide fuel cells *J. Power Sources* **472** 228606

[31] Chen Y *et al* 2017 A highly efficient and robust nanofiber cathode for solid oxide fuel cells *Adv. Energy Mater.* **7** 1601890

[32] Chen Y *et al* 2016 A durable, high-performance hollow-nanofiber cathode for intermediate-temperature fuel cells *Nano Energy* **26** 90–99

[33] Koo J Y, Hwang S, Ahn M, Choi M, Byun D and Lee W 2016 Controlling the diameter of electrospun yttria-stabilized zirconia nanofibers *J. Am. Ceram. Soc.* **99** 3146–50

[34] Ahn M, Lee J and Lee W 2017 Nanofiber-based composite cathodes for intermediate temperature solid oxide fuel cells *J. Power Sources* **353** 176–82

[35] Ahn M, Hwang S, Han S, Choi M, Byun D and Lee W 2020 Porous an hollow nanofibers for solid oxide fuel cell electrodes *Korean J. Chem. Eng.* **37** 1371–8

[36] Kim C, Park H, Jang I, Kim S, Kim K, Yoon H and Paik U 2018 Morphologically well-defined $Gd_{0.1}Ce_{0.9}O_{1.95}$ embedded $Ba_{0.5}Sr_{0.5}Co_{0.8}Fe_{0.2}O_{3-\delta}$ nanofiber with an enhanced triple phase boundary as cathode for low-temperature solid oxide fuel cells *J. Power Sources* **378** 404–11

[37] Jeon Y, Myung J H, Hyun S H, Shul Y G and Irvine J T S 2017 Corn-cob like nanofibres as cathode catalysts for an effective microstructure design in solid oxide fuel cells *J. Mater. Chem.* A **5** 3966–73

[38] Yang J M, Wang J K, Fu L, Wu K, Liu Z R, Wu K and Zhou J 2021 Electrospun core–shell fibers for high-efficient composite cathode-based solid oxide fuel cells *Energy Fuels* **35** 1768–78

[39] Lee J G, Park J H and Shul Y G 2014 Tailoring gadolinium-doped ceria-based solid oxide fuel cells to achieve 2 W cm^{-2} at 550 °C *Nat. Commun.* **5** 4045

[40] Ahn M, Cho J and Lee W 2019 One-step fabrication of composite nanofibers for solid oxide fuel cell electrodes *J. Power Sources* **434** 226749

[41] Chen Y *et al* 2018 A robust fuel cell operated on nearly dry methane at 500 °C enabled by synergistic thermal catalysis and electrocatalysis *Nat. Energy* **3** 1042–50

[42] Bellino M G, Sacanell J G, Lamas D G, Leyva A G and De Reca N E W 2007 High-performance solid-oxide fuel cell cathodes based on cobaltite nanotubes *J. Am. Chem. Soc.* **129** 3066–7

[43] Witz G, Shklover V, Steurer W, Bachegowda S and Bossmann H P 2007 Phase evolution in yttria-stabilized zirconia thermal barrier coatings studied by rietveld refinement of x-ray powder diffraction patterns *J. Am. Ceram. Soc.* **90** 2935–40

[44] Kilo M, Argirusis A, Borchardt G and Jackson R A 2003 Oxygen diffusion in yttria stabilised zirconia—experimental results and molecular dynamics calculations *Phys. Chem. Chem. Phys.* **5** 2219–24

[45] Dos Santos-Gómez L, Losilla E R, Martín F, Ramos-Barrado J R and Marrero-López D 2015 Novel

[46] Zhang X M, Liu L, Zhao Z, Tu B F, Ou D R, Cui D A, Wei X M, Chen X B and Cheng M J 2015 Enhanced oxygen reduction activity and solid oxide fuel cell performance with a nanoparticles-loaded cathode *Nano Lett.* **15** 1703–9

[47] Yu K, Lou L L, Liu S X and Zhou W Z 2020 Asymmetric oxygen vacancies: the intrinsic redox active sites in metal oxide catalysts *Adv. Sci.* **7** 1901970

[48] Yu K *et al* 2018 *The role of Bi-doping in promoting electron transfer and catalytic performance of $Pt/3DOM\text{-}Ce_{1-x}Bi_xO_{2-\delta}$* *J. Catal.* **365** 292–302

[49] Wei T, Singh P, Gong Y H, Goodenough J B, Huang Y H and Huang K 2014 $Sr_{3-3x}Na_{3x}Si_3O_{9-1.5x}$ (x = 0.45) as a superior solid oxide-ion electrolyte for intermediate temperature-solid oxide fuel cells *Energy Environ. Sci.* **7** 1680–4

[50] Zhang W W, Wang H C, Guan K, Wei Z Y, Zhang X, Meng J L, Liu X J and Meng J 2019 $La_{0.6}Sr_{0.4}Co_{0.2}Fe_{0.8}O_{3-\delta}/CeO_2$ heterostructured composite nanofibers as a highly active and robust cathode catalyst for solid oxide fuel cells *ACS Appl. Mater. Interfaces* **11** 26830–41

[51] Yoon K J, Biswas M, Kim H J, Park M, Hong J, Kim H, Son J W, Lee J H, Kim B K and Lee H W 2017 Nano-tailoring of infiltrated catalysts for high-temperature solid oxide regenerative fuel cells *Nano Energy* **36** 9–20

[52] Kim J *et al* 2021 Naturally diffused sintering aid for highly conductive bilayer electrolytes in solid oxide cells *Sci. Adv.* **7** eabj8590

[53] Kim C, Kim S, Jang I, Yoon H, Song T and Paik U 2019 Facile fabrication strategy of highly dense gadolinium-doped ceria/yttria-stabilized zirconia bilayer electrolyte via cold isostatic pressing for low temperature solid oxide fuel cells *J. Power Sources* **415** 112–8

[54] Wang S Z, Jin F J, Li L, Li R R, Qu B P and He T M 2017 Stability, compatibility and performance improvement of $SrCo_{0.8}Fe_{0.1}Nb_{0.1}O_{3-\delta}$ perovskite as a cathode for intermediate-temperature solid oxide fuel cells *Int. J. Hydrog. Energy* **42** 4465–77

[55] Yoo S, Jun A, Ju Y W, Odkhuu D, Hyodo J, Jeong H Y, Park N, Shin J, Ishihara T and Kim G 2014 Development of double-perovskite compounds as cathode materials for low-temperature solid oxide fuel cells *Angew. Chem.* **126** 13280–3

[56] Lim C, Sengodan S, Jeong D, Shin J and Kim G 2019 Investigation of the Fe doping effect on the B-site of the layered perovskite $PrBa_{0.8}Ca_{0.2}Co_2O_{5+\delta}$ for a promising cathode material of the intermediate-temperature solid oxide fuel cells *Int. J. Hydrog. Energy* **44** 1088–95